Nanoscale Advances

ROYAL SOCIETY OF CHEMISTRY

PAPER

View Article Online
View Journal | View Issue

Cite this: *Nanoscale Adv.*, 2024, **6**, 5612

A 2D hybrid nanocomposite: a promising anode material for lithium-ion batteries at high temperature†

Bongu Chandra Sekhar, [a] Abdelrahman Soliman,[a] Muhammad Arsalan[b] and Edreese H. Alsharaeh *[a]

Two-dimensional atomically thick materials including graphene, BN, and molybdenum disulfide (MoS_2) have been investigated as possible energy storage materials, because of their large specific surface area, potential redox activity, and mechanical stability. Unfortunately, these materials cannot reach their full potential due to their low electrical conductivity and layered structural restacking. These problems have been somewhat resolved in the past by composite electrodes composed of a graphene and MoS_2 mixture; however, insufficient mixing at the nanoscale still limits performance. Here, we examined lithium-ion battery electrodes and reported three composites made using a basic ball milling technique and sonication method. The 5% BN-G@MoS_2-50@50 composite obtained has a homogeneous distribution of MoS_2 on the graphene sheet and H-BN with high crystallinity. Compared to the other two composites (5% BN-G@MoS_2-10@90 and 5% BN-G@MoS_2-90@10), the 5% BN-G@MoS_2-50@50 composite electrode exhibits a high specific capacity of 765 mA h g^{-1} and a current density of 100 mA g^{-1} in batteries. Additionally, the 5% BN-G@MoS_2-50@50 composite electrode displays an excellent rate capability (453 mA h g^{-1} at a current density of 1000 mA g^{-1}) at a high temperature of 70 °C, thanks to h-BN that allows reliable and safe operation of lithium-ion batteries. Our research may pave the way for the sensible design of different anode materials, including 2D materials (5% BN-G@MoS_2-50@50) for high-performance LIBs and other energy-related fields.

Received 21st May 2024
Accepted 24th July 2024

DOI: 10.1039/d4na00424h

rsc.li/nanoscale-advances

1. Introduction

A significant challenge today is meeting the world's energy needs while maintaining a healthy balance between the quantity of energy produced and consumed. Non-renewable resources are currently the main source of energy generation.[1] Because they are more readily available, easier to mine and transport, and more practical for use in homes, businesses, and industries, fossil fuels including coal, oil, and natural gas are frequently employed as key energy sources.[2,3] On the other hand, the burning of fossil fuels is considered the main source of greenhouse gas emissions, particularly carbon dioxide, which is the primary cause of global warming and the ensuing climate change.[4] Furthermore, the move toward renewable energy sources has been prompted by their limited nature and ongoing depletion as a result of heavy reliance.[5] Because they produce the fewest greenhouse gas emissions, renewable energy sources such as solar, hydropower, geothermal, wind, and biomass are growing in popularity.[6–8] These energy sources are acknowledged as sustainable substitutes. Many countries have switched to using renewable energy sources to provide electricity.[9]

Lithium-ion batteries (LIBs), the most promising energy conversion and storage technology, are used extensively in hybrid electric vehicles (HEVs) and portable gadgets because of their high energy densities.[10–14] Other electro-active materials have been investigated as potential replacements for the existing carbonaceous anode with a restricted theoretical capacity of 372 mA h g^{-1} to meet long cycle life and rate stability requirements. Since the discovery of graphene, 2D materials have drawn much attention, particularly because of the many changes in their chemical and physical properties. Two-dimensional (2D) materials have become increasingly popular over time, particularly for energy storage applications. Examples include MXenes, transition metal oxides (TMOs), transition metal dichalcogenides (TMDs), transition metal carbides and nitrides, hexagonal boron nitride (h-BN), 2D metal–organic frameworks (MOFs), borophene, and so forth.[15–21] Certain materials, including transition metal sulfides (TMSs), have garnered interest because of their safety, high energy density, and high capacity.[22–27] Because of their inherent safety and potential applications, TMSs have emerged as the most

[a]College of Science and General Studies, AlFaisal University, PO Box 50927, Riyadh, 11533, Saudi Arabia. E-mail: ealsharaeh@alfaisal.edu

[b]EXPEC Advanced Research Center, Saudi Aramco, P.O. Box 5000, Dhahran, 31311, Saudi Arabia

† Electronic supplementary information (ESI) available. See DOI: https://doi.org/10.1039/d4na00424h

appealing anode materials for LIBs compared to a few other promising materials.

Due to their intriguing physical and chemical characteristics, TMS materials like MoS_2 and WS_2 have found extensive application in lithium-ion batteries (LIBs), sodium-ion batteries (NIBs), photocatalysis, electrocatalysis, supercapacitors, and sensors.[28–31] MoS_2 shares a layered structure with graphite and has a theoretical capacity that is roughly twice as high (670 mA h g^{-1}) as that of graphite.[32] Weak van der Waals interactions hold the layers together in MoS_2, but they are stronger than those in graphite (interlayer distance ~0.6 nm) in the case of Li-ion intercalation/deintercalation.[33,34] Its practical application is hindered by structural deterioration caused by a significant volume change upon charge/discharge and low intrinsic electrical conductivity between two adjacent S–Mo–S sheets.[35] These factors combined result in poor cycling performance and inferior rate capability. It has been shown that integrating nanostructured MoS_2 with conductive and flexible materials is an efficient way to increase electrochemical performance and overcome these limitations. The electrical conductivity and structural stability of the MoS_2 electrode material improved during cycling by combining MoS_2 with carbonaceous materials, such as graphene, carbon fibers, amorphous carbon, porous carbon, carbon spheres, or carbon nanotubes.[36–43] A carbon component can improve the MoS_2 electronic conductivity while buffering its volume changes throughout the lithiation/delithiation cycle, resulting in stable cycling performance and quick electrode kinetics. Because of its high specific surface area, superior mechanical qualities, and high electrical conductivity, graphene has garnered significant interest among numerous carbonaceous materials.[44] Numerous MoS_2/graphene composites in various morphologies were previously created.[32,34,36,40,45–48]

Hexagonal boron nitride (h-BN), a 2D material similar to graphene and molybdenum disulfide (MoS_2), is another example. Researchers' attention has been drawn to hexagonal and cubic boron nitride in particular. In contrast to graphene, which is formed of sp^2 hybridization, hexagonal boron nitride (h-BN) has a hexagonal crystal structure with boron and nitrogen atoms arranged in a honeycomb pattern.[49,50] It has been demonstrated that h-BN may be used as a polymer filler in a range of applications, including electrical and biological ones. It possesses high hydrophobicity, excellent mechanical strength, high hydrophobicity, strong thermal conductivity, non-toxicity, good thermal stability, and a good band gap of 6 eV.[51,52] The dielectric constant, thermal expansion coefficient, and moisture absorption capacity of h-BN make it a preferred material in light-emitting devices, the electronics industry, surface coating, nanoelectronics, and lubricants.[53] Despite having inferior electrical conduction, moisture absorption capacity, and thermal expansion coefficients, h-BN materials are primarily utilized in the electronics sector. Furthermore, because of their important properties such as transparency, excellent charge carrier mobility, edge configuration, sp^2 hybridization, size reduction, large surface area, high stability, and point vacancies, which guarantee good electrochemical performance of the electrode material, h-BN materials are better used in energy storage systems (electrodes and electrolytes).[54–63] The h-BN act as a filler to the graphene and MoS_2 to avoid the agglomeration and interlayer interactions for the composites. Consequently, MoS_2 and graphene combined with h-BN would undoubtedly be a good option for next-generation batteries.

Here, we show how to easily manufacture a BN-G@MoS_2 composite using h-BN, MoS_2, and graphene for use as a lithium-ion battery anode. A ball milling technique has been utilized to prepare the compositions of 5% BN_G@MoS_2_50@50, 5% BN_G@MoS_2_90@10, and 5% BN-G@MoS_2-10@90. Out of the three composites, the best performing composite (5% BN-G@MoS_2-50@50) has a high specific capacity of 765 mA h g^{-1} and a 99.4% retention rate at a current density of 100 mA g^{-1} for 200 cycles. Motivated by these findings, a lithium-ion battery exhibits exceptional reversible capacity, achieving 440 mA h g^{-1} at a 1000 mA g^{-1} rate with a 97% coulombic efficiency for 500 cycles. Additionally, the 5% BN-G@MoS_2-50@50 composite electrode exhibits high-rate capability and coulombic efficiency even at high temperature. As-prepared, the 5% BN-G@MoS_2-50@50 composite is anticipated to be a good option for the anode of next-generation, high-performance lithium-ion batteries.

2. Experimental section

2.1. Materials

Na_2S and $(NH_4)_2MoO_4$ (about 99.98%) and *N*-methyl-2-pyrrolidone (99.9%) were purchased from Merck. MTI Corporation provided poly(vinylidene fluoride) powder and 50% compressed carbon black. h-BN with 98% purity and 99.9999% graphene powder were bought from Graphene Supermarket and XG Sciences. Alcohol and hydrochloric acid were acquired from local companies for washing purposes. All the chemicals were used without any further purification.

2.2. Material synthesis

2.2.1. Preparation of MoS_2. MoS_2 was prepared using a simple ball milling method (Scheme 1). Firstly, 1 g of Na_2S and 0.35 g of $(NH_4)_2MoO_4$ were added and stirred in a few ml of distilled water for 1 hour. The aforementioned aqueous solution is mixed with the required amount of hydrochloric acid (HCl) to create the amorphous precursor of MoS_2. The dried precursor was then vigorously ball-milled in a planetary ball mill for 24 hours at 500 rpm in an Ar environment. Balls made of stainless steel served as the milling medium. Finally, to eliminate byproducts, the ball-milled product was repeatedly rinsed with deionized water, alcohol, and hydrochloric acid. After collecting the final molybdenum disulfide, it was dried for 12 hours at 60 °C.

2.2.2. Preparation of h-BN/graphene/MoS_2 composites. The preparation of h-BN/graphene/MoS_2 composites has been reported previously,[61] but here a more detailed explanation is provided. Graphene and the prepared MoS_2 were used as starting materials to create MoS_2/graphene (50 : 50, 10 : 90, and 90 : 10) nanocomposites using ball milling and sonication in the first stage. Following a 30 minute grinding period, the

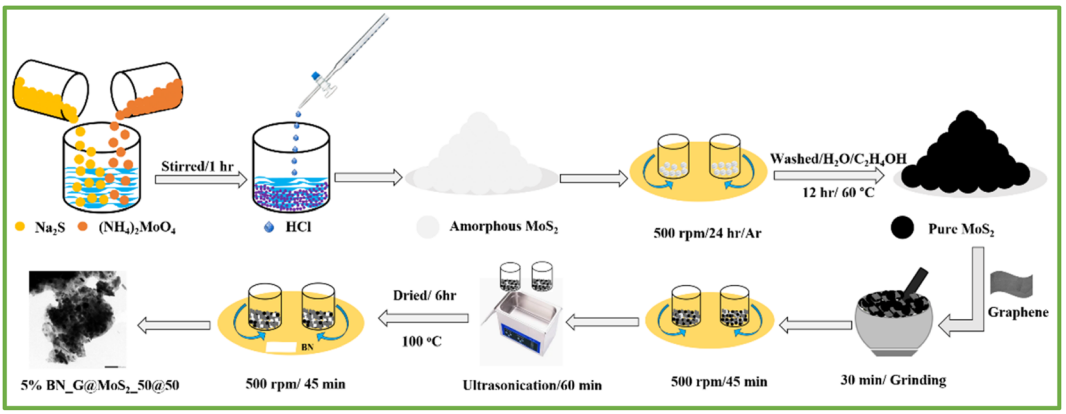

Scheme 1 Schematic illustration of the preparation process of pure MoS_2 and composite anode materials.

powdered graphene and MoS_2 were subjected to 45 minutes of ball milling at varying ratios (50 : 50, 10 : 90, and 90 : 10) (powder weight ratio with balls to material: 4 : 1 at 1060 rotational speed (rpm)) utilizing a SPEX samplePrep P instrument (Model number 8000M MIXER/MILL) with two distinct ball sizes (four 6.3 mm and two 12.5 mm stainless steel balls). Ethanol (25 mL) was subjected to ultrasonication (250 W, 20 kHz, model VWR Ultrasonic Cleaner USC THD instrument) for 60 minutes at room temperature in order to achieve better homogeneity. The produced MoS_2@graphene nanohybrid was dried for six hours at 100 °C in a vacuum furnace. After 45 minutes of ball milling with 5 weight percent of BN, MoS_2 with graphene composites (50 : 50, 10 : 90, and 90 : 10) were ultrasonicated for 60 minutes to improve homogeneity. The finished products 5% BN_G@MoS_2_50@50, 5% BN_G@MoS_2_90@10, and 5% BN_G@MoS_2_10@90 were produced by ultrasonically sonicating the material and then drying it for six hours at 100 °C in a vacuum furnace.

3. Characterization

3.1. Physicochemical characterization

A Rigaku Miniflex 600 X-ray diffractometer was used to study the crystalline nature and phase composition of the prepared composites using CuKa radiation ($l = 1.5406$). The morphology of the prepared composite materials was studied by using Gemini Scanning Electron Microscopy (SEM) and transmission electron microscopy (TEM). In the sample preparation for TEM analysis, the composite samples were ultra-sonicated for 20 min in a mixed solution of ethanol and water, followed by drop-casting onto a fresh lacey carbon copper grid.

3.2. Electrochemical characterization

The electrochemical performance tests including cyclic voltammetry (CV), galvanostatic current charge–discharge (GCD) and electrochemical impedance spectroscopy (EIS) methods (AC voltage of 5 mV) in a two-electrode system were implemented by using a Bio-Logic SP-300 Modular electrochemical workstation. 5% BN-G@MoS_2-10@90, 5% BN-G@MoS_2-50@50 and 5% BN-G@MoS_2-90@10 were used to fabricate the working electrodes. The composite samples (BN-G@MoS_2) were mixed with carbon black (Super-P) and poly(vinyl difluoride) (PVDF) in a weight ratio of 80 : 10 : 10 and coated on copper foil using a doctor blade (MTI Corporation) and dried at 80 °C for 12 h in a vacuum oven. The mass loading of the electrode materials on the foil (15 mm) was 1.0–1.5 mg. Li foils were used as the counter/reference electrodes for half-cell fabrication. Polypropylene was utilized as the separator, and the electrolyte was 1 M $LiPF_6$ dissolved in ethylene carbonate (EC)/dimethyl carbonate (DMC) (1 : 1 by volume). Coin cells (CR2032) with Li foil as the cathode and composites as anodes were assembled in an Ar-filled glove box to test the electrochemical performance of the as-prepared electrodes. High-temperature studies were conducted using a bomb calorimeter vessel connected to a Gamry electrochemical working station. High-temperature tests were performed for long-term cycling at 70 °C using coin cells through a constant-current process with a current density of 500 mA g^{-1}. The potential window applied was 0.01 to 3.0 V. The loading of the electrode material (5% BN-G@MoS_2-50@50) was 1.0 mg.

4. Results and discussion

By using X-ray diffraction (XRD), the crystalline structures of the as-prepared materials, MoS_2 and composites (5% BN-G@MoS_2-10@90, 5% BN-G@MoS_2-50@50, and 5% BN-G@MoS_2-90@10), were investigated and the results are plotted in Fig. S1† and 1. The unique diffraction peaks at 2θ angels of approximately 14.0°, 33.1°, 39.2°, 43.7°, 49.5°, 58.4°, and 60.1°, respectively, correspond to the MoS_2 hexagonal (JCPDS card No. 37-1492) phase crystal planes (002), (100), (103), (006), (110), and (008).[42] Furthermore, when graphite (002) is present, the XRD patterns of the 5% BN-G@MoS_2-10@90, 5% BN-G@MoS_2-50@50, and 5% BN-G@MoS_2-90@10 composites exhibit a peak at 26.8°. Additionally, the peak of 5% BN-G@MoS_2-90@10 is more visible at around 26.8° than those of 5% BN-G@MoS_2-10@90 and 5% BN-G@MoS_2-50@50 composites. This suggests that the higher graphene content of 5% BN-G@MoS_2-90@10 is consistent with the synthesis process, as is the case with 5% BN-G@MoS_2-10@90 and 5% BN-G@MoS_2-50@50 composites. Nevertheless,

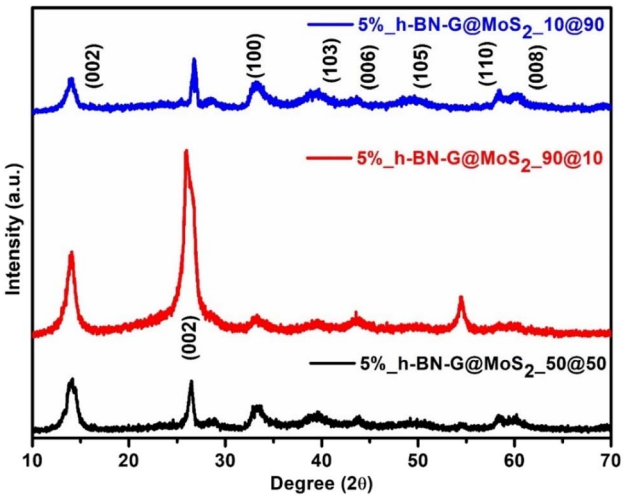

Fig. 1 XRD patterns of 5% BN-G@MoS_2-10@90, 5% BN-G@MoS_2-50@50 and 5% BN-G@MoS_2-90@10 materials.

the peak intensity of the 5% BN-G@MoS_2-10@90 and 5% BN-G@MoS_2-50@50 composites is greatly reduced due to the reduction in crystallinity (calculated using Debye Scherrer's equation (eqn (1))) and the S–Mo–S layer number. The crystal sizes of the 5% BN-G@MoS_2-90@10, 5% BN-G@MoS_2-50@50, and 5% BN-G@MoS_2-90@10 composites were 74, 72 and 60 nm, respectively.

$$\text{Debye Scherrer's equation} = D = \frac{K \times \lambda}{\beta \cos \theta} \quad (1)$$

where D = crystallite size, K = Scherrer constant (0.9), λ = wavelength of the X-rays used (0.15406 nm), β = full width at half maximum (FWHM, radians), and θ = peak position (radians).

Scanning electron microscopy was used to methodically examine the morphology of the prepared 5% BN-G@MoS_2-10@90, 5% BN-G@MoS_2-90@10, and 5% BN-G@MoS_2-50@50 composites (Fig. 2). SEM images unequivocally indicate that the ratios of graphene to MoS_2 have a significant impact on the morphology of the compositions. The 5% BN-G@MoS_2-10@90 composition is depicted in Fig. 2a–c, where MoS_2 is not completely covered by the graphene substrate network and exhibits self-aggregation. However, 5% BN-G@MoS_2-90@10 and 5% BN-G@MoS_2-50@50 composites are shown in Fig. 2d–i. Fig. 2g–i show the low to high magnification SEM images of the 5% BN-G@MoS_2-50@50 composite, respectively. It is evident from the high magnification image that the graphene sheets include both h-BN and MoS_2. However, transmission electron microscopy (TEM) analysis was carried out for pure MoS_2 and 5% BN-G@MoS_2-50@50 composite materials (Fig. S2† and 3). From TEM, the MoS_2 particles are nanosized. The composite material shown in Fig. 3 reveals that every single MoS_2 particle has a graphene coating. The enlarged views of Fig. 3c and d show how individual MoS_2 is present in conjunction with graphene to inhibit aggregation and limit the volume increase that is unavoidable. In the 5% BN-G@MoS_2-50@50 nanocomposite, in particular, MoS_2 was evenly distributed and well-integrated onto the graphene sheet, preventing the nanosheets from aggregating due to the composition.

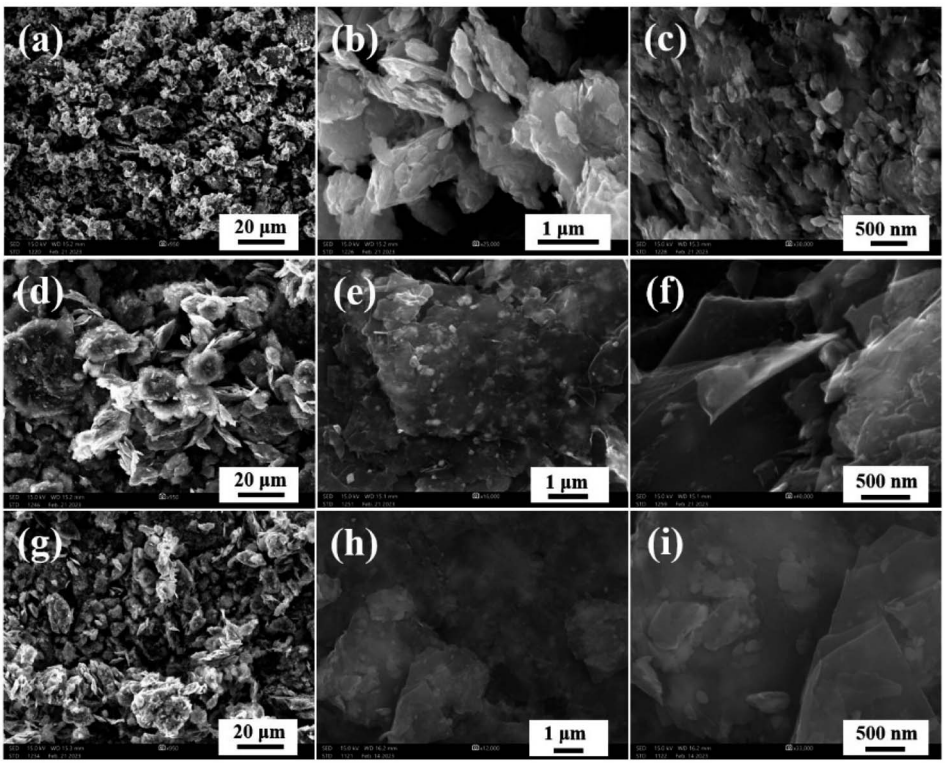

Fig. 2 SEM images of (a–c) 5% BN-G@MoS_2-10@90, (d–f) 5% BN-G@MoS_2-90@10 and (g–i) 5% BN-G@MoS_2-50@50 materials.

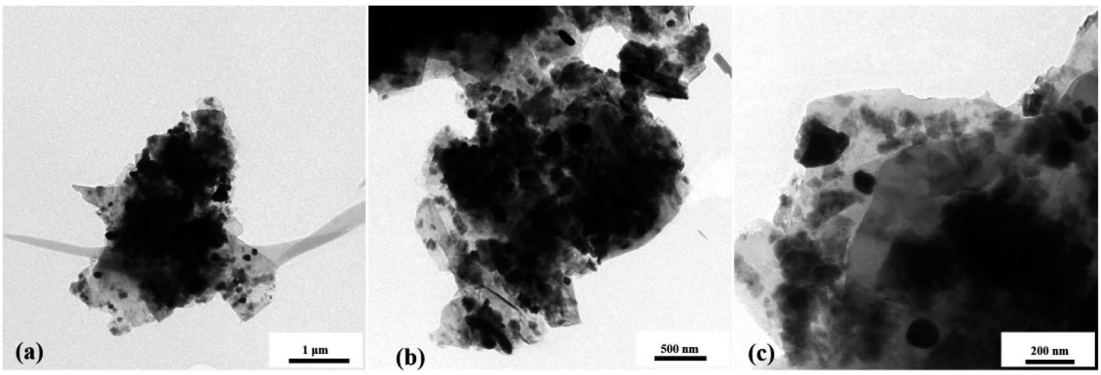

Fig. 3 TEM images of (a–c) 5% BN-G@MoS_2-50@50 composite material.

4.1. Electrochemical characterization

4.1.1. Half-cell electrochemical performance at room temperature. The BN-G@MoS_2 composites were studied as potential anode materials for lithium-ion batteries to assess their electrochemical characteristics. Cyclic voltammetry (CV) measurements were performed at a scan rate of 0.05 mV s^{-1} in the potential range of 0.01–3.0 V to assess the electrochemical activity of composite electrodes with 5% BN-G@MoS_2-10@90, 5% BN-G@MoS_2-90@10, and 5% BN-G@MoS_2-50@50. The recorded curves of the three samples are similar and displayed in Fig. 4. Particularly, three cathodic peaks can be seen in the first cycle at roughly 1.25 V, 0.68 V and 0.52 V. The tiny peak at about 1.25 V is due to Li^+ intercalation into the MoS_2 layered structure, which results in Li_xMoS_2. This is accompanied by a phase transition of $LixMoS_2$ from the 2H to 1T structure.[36,38,64] The additional conversion reaction from Li_xMoS_2 into metallic Mo and Li_2S is responsible for the 0.68 V peak. Thus, the continuous reaction with the electrolyte solution to generate a SEI film could be the cause of the 0.52 V peak. Two peaks may be seen in the anodic scans at 1.75 V and 2.36 V for the 5% BN-G@MoS_2-50@50 composite. It is possible to attribute the faint and broad peak at 1.75 V to Mo's partial oxidation to MoS_2 (Mo

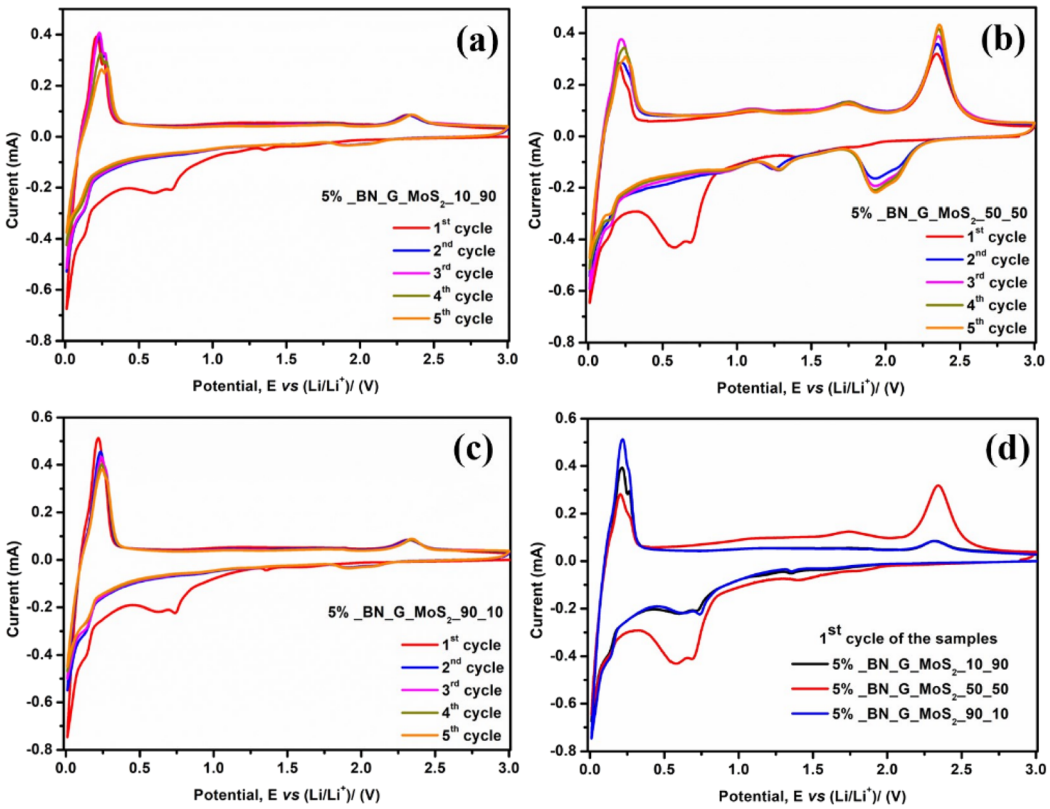

Fig. 4 (a–c) Cyclic voltammograms of 5% BN-G@MoS_2-10@90, 5% BN-G@MoS_2-50@50 and 5% BN-G@MoS_2-90@10 anodes at a scan rate of 0.05 mV s^{-1} and (d) 1st CV cycle curves of the 5% BN-G@MoS_2-10@90, 5% BN-G@MoS_2-50@50 and 5% BN-G@MoS_2-90@10 anodes.

to Mo^{4+}/Mo^{6+}). The production of sulfur is shown by the prominent oxidation peak at 2.36 V (Li_2S to sulfur or polysulfides).[65,66] However, 5% BN-G@MoS_2-10@90 (Fig. 4a) and 5% BN-G@MoS_2-90@10 (Fig. 4c) composite electrodes show one oxidation peak at 2.36 V with lower current intensity than the 5% BN-G@MoS_2-50@50 composite electrode (Fig. 4b and d). One reduction peak at 1.98 V and one oxidation peak at 2.34 V are seen from the second to the fifth cycle, and they do not clearly differ from one another, indicating that the composite electrodes made of 5% BN-G@MoS_2-10@90 and 5% BN-G@MoS_2-90@10 exhibit good stability. More significantly, it is evident that the G coating layer helps host the electrochemical products of Mo and soluble lithium polysulfides. This is because the oxidation peak at 2.34 V, corresponding to the delithiation of Li_2S and Mo, is observed in 5% BN-G@MoS_2-50@50. Additionally, it should be noted that cycling causes the intensity of the oxidation peak at 2.34 V to rise slightly, suggesting that the activation process is still happening.[32]

To determine the lithium storage capacity of the 5% BN-G@MoS_2-10@90, 5% BN-G@MoS_2-90@10, and 5% BN-G@MoS_2-50@50 composite electrodes, galvanostatic charge/discharge cycle experiments were performed at different current densities from 50 to 1000 mA g^{-1} and the results are shown in Fig. 5a. In Fig. 5a, the 5% BN-G@MoS_2-50@50 composite electrode shows a superior rate capability to the 5% BN-G@MoS_2-10@90 and 5% BN-G@MoS_2-90@10 composite electrodes. At current densities of 50 mA g^{-1}, 100 mA g^{-1}, 200 mA g^{-1}, 400 mA g^{-1}, 500 mA g^{-1}, 800 mA g^{-1} and 1000 mA g^{-1}, respectively, the measured reversible discharge capacities of the 5% BN-G@MoS_2-50@50 composite electrode are 1462 mA h g^{-1}, 798 mA h g^{-1}, 698 mA h g^{-1}, 593 mA h g^{-1}, 529 mA h g^{-1}, 473 mA h g^{-1} and 397 mA h g^{-1}. The composite anode regains its initial specific capacity of 1023 mA h g^{-1}, demonstrating the exceptional reversibility of the 5% BN-G@MoS_2-50@50 anode when the current density drops to 50 mA g^{-1}. In contrast, the electrodes with 5% BN-G@MoS_2-10@90 and 5% BN-G@MoS_2-90@10 exhibit rapid capacity fading when the C-rate rises from 50 mA g^{-1} to 1000 mA g^{-1}. The reversible capacities of the 5% BN-G@MoS_2-10@90 composite electrode are 730 mA h g^{-1}, 364 mA h g^{-1}, 227 mA h g^{-1}, 141 mA h g^{-1}, 135 mA h g^{-1}, 99 mA h g^{-1} and 91 mA h g^{-1} at current densities of 50 mA g^{-1}, 100 mA g^{-1}, 200 mA g^{-1}, 400 mA g^{-1}, 500 mA g^{-1}, 800 mA g^{-1} and 1000 mA g^{-1}, respectively. The 5% BN-G@MoS_2-50@50 composite electrode shows a capacity 2 and 3 times higher than the 5% BN-G@MoS_2-10@90 and 5% BN-G@MoS_2-90@10 composite electrodes at a current density of 50 mA g^{-1}, respectively. The 5% BN-G@MoS_2-50@50 composite electrode

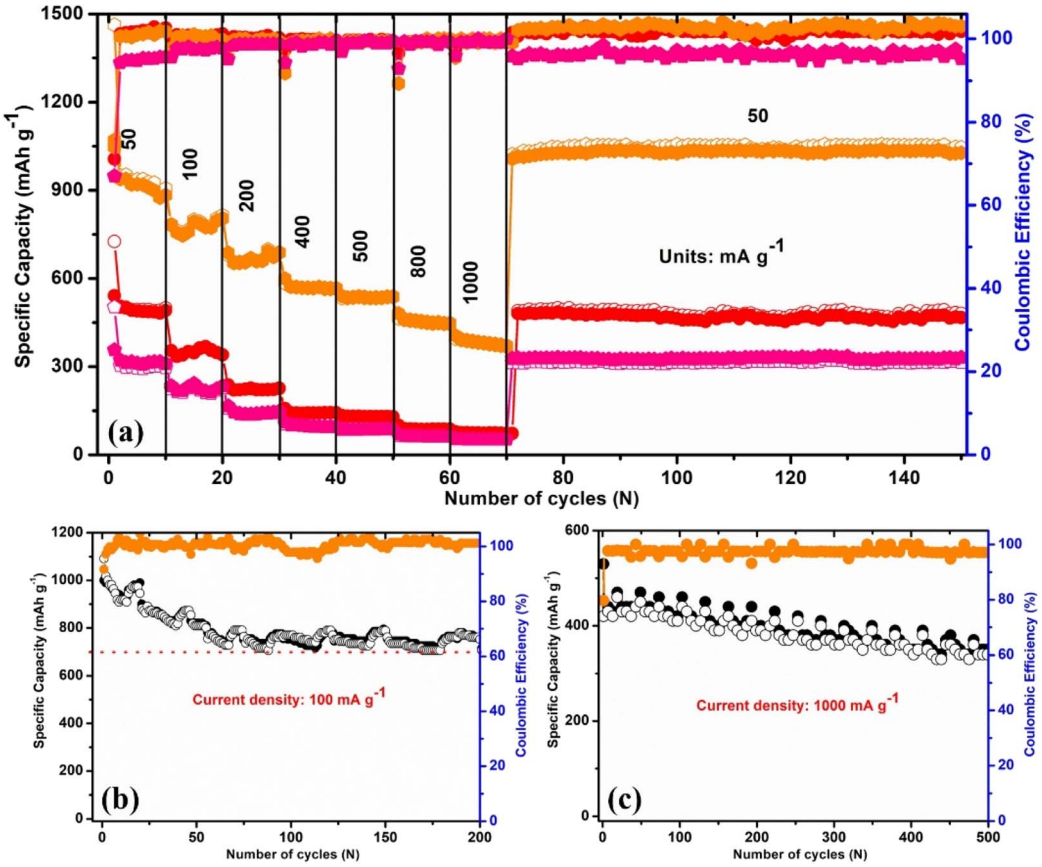

Fig. 5 (a) Rate capability (50 to 1000 mA g^{-1}) and long-term cycling performance at 50 mA g^{-1} of 5% BN-G@MoS_2-10@90, 5% BN-G@MoS_2-50@50, and 5% BN-G@MoS_2-90@10 composite electrodes, and long-term cycling performance and coulombic efficiencies of the 5% BN-G@MoS_2-50@50 composite electrode tested at current densities of (b) 100 mA g^{-1} and (c) 1000 mA g^{-1}.

then exhibits a high average specific capacity of 1050 mA h g^{-1} when the test current density is reduced back to 50 mA g^{-1}. This compound's specific capacity is greater than those of the 5% BN-G@MoS_2-90@10 and 5% BN-G@MoS_2-10@90 compounds (485 and 320 mA h g^{-1}). The remarkable improvements observed for the 5% BN-G@MoS_2-50@50 composite at high rates show that the electrical and ionic conductivities have greatly improved, in addition to the structural stability, which has been greatly enhanced. Furthermore, the rate performance has been investigated along with the long-term cycling stability at a high current density of 50 mA g^{-1}. It is evident that after 70 cycles (Fig. 5a), the 5% BN-G@MoS_2-50@50 composite electrode can maintain a capacity of 1035 mA h g^{-1}, whereas the 5% BN-G@MoS_2-10@90 and 5% BN-G@MoS_2-90@10 composite electrodes are nearly at the point of failure. The capacity of the 5% BN-G@MoS_2-10@90 and 5% BN-G@MoS_2-90@10 composite electrodes rapidly decreases, most likely due to poor conductivity and significant structural damage from volume changes that pulverize the active material.

5% BN-G@MoS_2-10@90, 5% BN-G@MoS_2-50@50, and 5% BN-G@MoS_2-90@10 have initial charge and discharge capacities of 505/730 mA h g^{-1}, 1070/1462 mA h g^{-1}, and 356/502 mA h g^{-1}, respectively, at 50 mA g^{-1} current density. These values correspond to the respective coulombic efficiencies of 73.0%, 71.0%, and 67.0%. The enhanced capacity and efficiency of the 5% BN-G@MoS_2-50@50 electrode can be attributed to the homogeneous dispersion of MoS_2 on the conductive graphene network. Evidently, the development of the SEI layer is what causes the irreversible capacity loss that occurs during the first cycle.[36]

The coulombic efficiency of the 5% BN-G@MoS_2-50@50 electrode steadily rises to around 99% in the subsequent cycles, which is higher than that of the 5% BN-G@MoS_2-10@90 (98%) and 5% BN-G@MoS_2-90@10 electrodes (~95%). Notably, when charged/discharged at high current densities of 100 and 1000 mA g^{-1}, the 5% BN-G@MoS_2-50@50 electrode shows a remarkable long-term cycling performance as well, as shown in Fig. 5b and c. Fig. 5b clearly shows that after 200 cycles the 5% BN-G@MoS_2-50@50 electrode exhibits 758 mA h g^{-1} at 100 mA g^{-1}, which is double the theoretical capacity of commercial graphite anodes (Fig. S3†) and higher than values reported in previous publications for lithium-ion batteries (Table 1). However, the 5% BN-G@MoS_2-50@50 electrode exhibits three times higher capacity than pure MoS_2 (Fig. S4†) and fifteen times higher capacity than the h-BN electrode material (Fig. S5†). Another cell test at a current density of 1000 mA g^{-1} confirms the 5% BN-G@MoS_2-50@50 electrode composite's excellent cycle performance. As demonstrated in Fig. 5c, the 5% BN-G@MoS_2-50@50 composite electrode shows a reversible specific capacity of 485 mA h g^{-1} at 1000 mA g^{-1} after 500 cycles, which is still greater than that of the commercial graphite anode. On the other hand, the composite's high capacity and electrochemical stability result from graphene's control over the structural stability of MoS_2 and H-BN, which reversibly store charges through surface redox processes.[76]

Fig. 6a–c depict the charge/discharge curves of the 5% BN-G@MoS_2-10@90, 5% BN-G@MoS_2-50@50, and 5% BN-G@MoS_2-90@10 anodes at varying current densities. During the first cycle of the three composite electrodes, irreversible capacity loss occurs due to the formation of a solid electrolyte interface layer (SEI) and electrolyte breakdown (Fig. 6d). In the three composite electrodes, at low current density, electrode polarization decreases, indicating effective electron transfer and lithium diffusion. At high current rates, electrode polarisation increased, whereas discharge capacities declined dramatically, highlighting the negative influence of current density on specific capacity in the three composite electrodes. In the discharge/charge profiles of the 5% BN-G@MoS_2-50@50 composite (Fig. 6b), there are two plateaus: 1.99 and 1.52 V for discharge and 1.77 and 2.36 V for charging (Fig. 6d). The 5% BN-G@MoS_2-50@50 composite exhibits lower polarization and high plateaus in all the cycles compared to the other two composites (Fig. 6a and c), indicating its high structural stability due to graphene and H-BN.

Fig. 7 depicts the Nyquist plots (electrochemical impedance spectra, EIS) of 5% BN-G@MoS_2-10@90, 5% BN-G@MoS_2-50@50, and 5% BN-G@MoS_2-90@10 electrodes before (Fig. 7a) and after 150 discharge–charge cycles (Fig. 7b), which were used to study electrode kinetics and charge/discharge capacity changes before and after cycling. Before cycling, the Nyquist plot shows the electrolyte resistance (R_s) in the high-frequency

Table 1 Comparison of the electrochemical performance of the 5% BN-G@MoS_2-50@50 composite with previous publications

Anode materials	Current density	Reversible capacity (mA h g^{-1})	Ref.
MoS_2/3DGN	100 mA g^{-1}	877	27
MoS_2	100 mA g^{-1}	200	32
MoS_2	500 mA g^{-1}	737	67
MoS_2/Mo_2TiC_2Tx-500	100 mA g^{-1}	646	68
MoS_2/C	100 mA g^{-1}	650	69
G/UT- TiO_2@C-150/FL-MoS_2	100 mA g^{-1}	802 (100th cycle)	70
MoS_2/C-73	100 mA g^{-1}	600	71
MoS_2/graphite	150 mA g^{-1}	490	72
MoO_3@MoS_2	69 mA g^{-1}	590	73
MoS_2@Mo_2C	50 mA g^{-1}	150	74
MoS_2/MoO_3	200 mA g^{-1}	510	75
5%BN-G@MoS_2-50@50	**100 mA g^{-1}**	**758 (200th cycle)**	**This work**

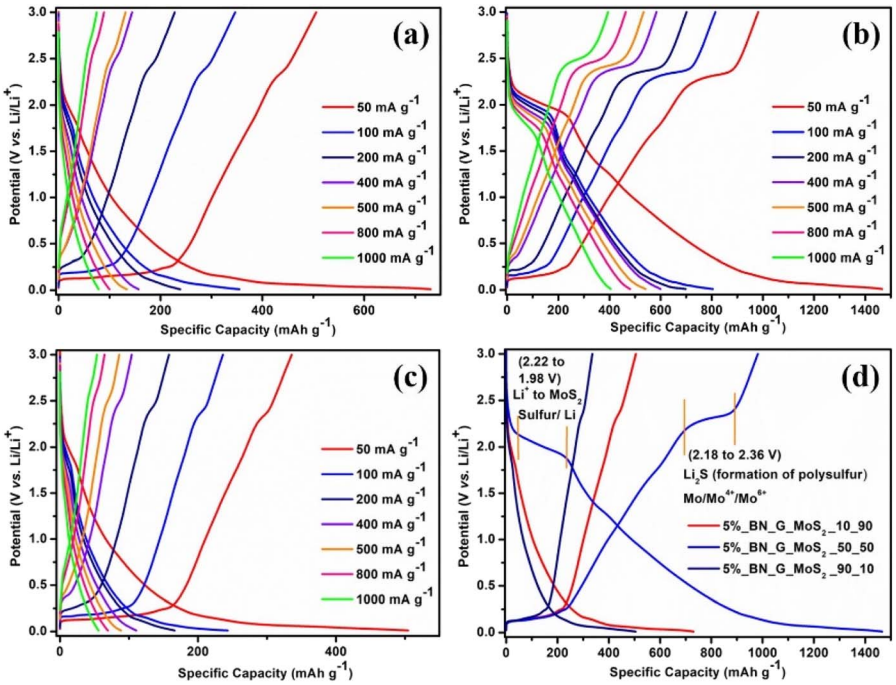

Fig. 6 Galvanostatic charge–discharge curves of (a) 5% BN-G@MoS_2-10@90, (b) 5% BN-5% BN-G@MoS_2-50@50, and (c) G@MoS_2-90@10 composite electrodes at different current rates and (d) GCD curves of the three composites at 50 mA g^{-1}.

range and the typical charge transfer resistance (R_{ct}) in the medium-low-frequency region with a spike in the low-frequency region (Li-ion diffusion into the electrode).[77] Another depressed semi-circle in the high to medium frequency band is shown in the Nyquist plot obtained after 150 cycles (Fig. 7b). The formation of the solid electrolyte interface (SEI) layer on the anodes is indicated by the comparatively small quasi-semi-circle in the high to medium frequency range. Compared to the 5% BN-G@MoS_2-10@90 anode (72 Ω), the 5% BN-G@MoS_2-50@50 (47 Ω) and 5% BN-G@MoS_2-90@10 anodes (38 Ω) exhibit smaller R_{ct} (Fig. 7a). The combination of graphene and MoS_2 components results in better reaction kinetics for quick electrochemical reactions, as evidenced by the lowered R_{ct}. It is important to remember that the redistribution of the active material within the matrix provides better contact, which lowers charge transfer and results in a cell with a resistance that is substantially lower after cycling than when the cell is freshly prepared.[78] The R_s of the 5% BN-G@MoS_2-50@50 electrode slightly increased to 9.9 Ω (compared to 8.9 Ω of the fresh cell) and R_{ct} decreased to 35.0 Ω (compared to 47.9 Ω of the fresh cell) after 150 cycles, as shown in Fig. 7b. Notably, the R_s and R_{ct} values of the 5% BN-G@MoS_2-10@90 anode and 5% BN-G@MoS_2-90@10 anode increased after 150 cycles (Table 1). Because of its better structure and electrode stability, the 5% BN-G@MoS_2-50@50 electrode exhibits outstanding electron transport kinetics that can be well maintained throughout

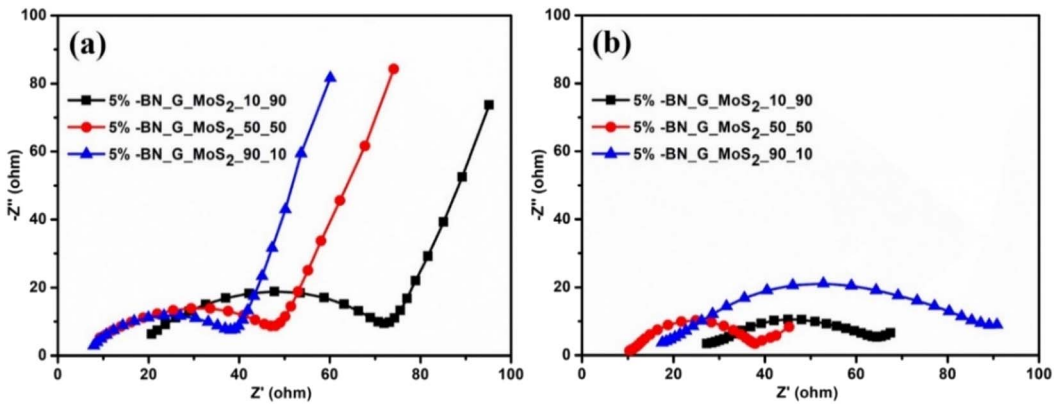

Fig. 7 Electrochemical impedance spectroscopy spectra of the as-fabricated (a) and after 150 cycles (b) of the 5% BN-G@MoS_2-10@90, 5% BN-G@MoS_2-50@50 and 5% BN-G@MoS_2-90@10 anodes.

repeated Li-ion insertion/extraction, as demonstrated by the above data. Based on the aforementioned data, the 5% BN-G@MoS_2-50@50 electrode exhibits the best LIB performance because it has superior structural stability, electron transport, and Li-ion transport properties to the 5% BN-G@MoS_2-90@10 electrode and the 5% BN-G@MoS_2-10@90 electrode.

4.1.2. Half-cell electrochemical performance at elevated temperature. The rate capability, discharge–charge curves, and impedance analysis of the 5% BN-G@MoS_2-50@50 composite electrode half cells at 70 °C are displayed in Fig. 8a–c. As illustrated in Fig. 8a, adequate electron transfer and lithium diffusion are indicated by the negligible electrode polarization at lower C-rates (*i.e.*, at 50, 100, and 200 mA g^{-1} current rates). Higher current rates (400–1000 mA g^{-1}) led to a considerable drop in discharge capacities and an increase in electrode polarization (Fig. 8b). The capacities of 929 mA h g^{-1} at 50 mA g^{-1} and 453 mA h g^{-1} at 1000 mA g^{-1} are attained with a rise in current density, demonstrating good rate capability even at high temperatures due to h-BN. A capacity of 1025 mA h g^{-1} remained after the current density dropped to 50 mA g^{-1}. The initial CE of the 5% BN-G@MoS_2-50@50 composite electrode is 131% at high temperatures. This is because of the uneven and thick surface, which reduces ion conductivity and causes irreversible capacity loss as well as unstable coulombic efficiency.[79–81] Following the fifth cycle, the CE of the composite electrode approaches 100% and remains constant throughout the battery cycling process. These findings show that, particularly at high temperatures, a stable SEI layer can form rapidly at the interface between the electrolyte and the 5% BN-G@MoS_2-50@50 composite electrode. Even at elevated temperatures, the lack of thermal damage to the cells demonstrates that the h-BN composite enables Li-ion batteries to operate dependably and safely.[82]

Fig. 8c displays the Nyquist plot of the 5% BN-G@MoS_2-50@50 composite electrode at room temperature and high temperature in the frequency range of 0.01 Hz to 100 kHz. R_s and R_{ct} values derived from the Nyquist plot are presented in Table 2. The R_s and R_{ct} values of the 5% BN-G@MoS_2-50@50 composite electrode were found to decrease as the temperature rose (Table 3). Reduced R_{ct} values indicate that the dynamic interface of the cell becomes more active at high temperatures and that the combination of G/MoS_2 and h-BN provides better reaction kinetics for rapid electrochemical reactions. After cycling, the electrode structure was studied using XRD and EIS analysis (Fig. S6 and S7†). XRD analysis shows the 5% BN-G@MoS_2-50@50 composite electrode structure did not change much but showed increased broadness. The impedance analysis of 5% BN-G@MoS_2-50@50 composite electrode before and

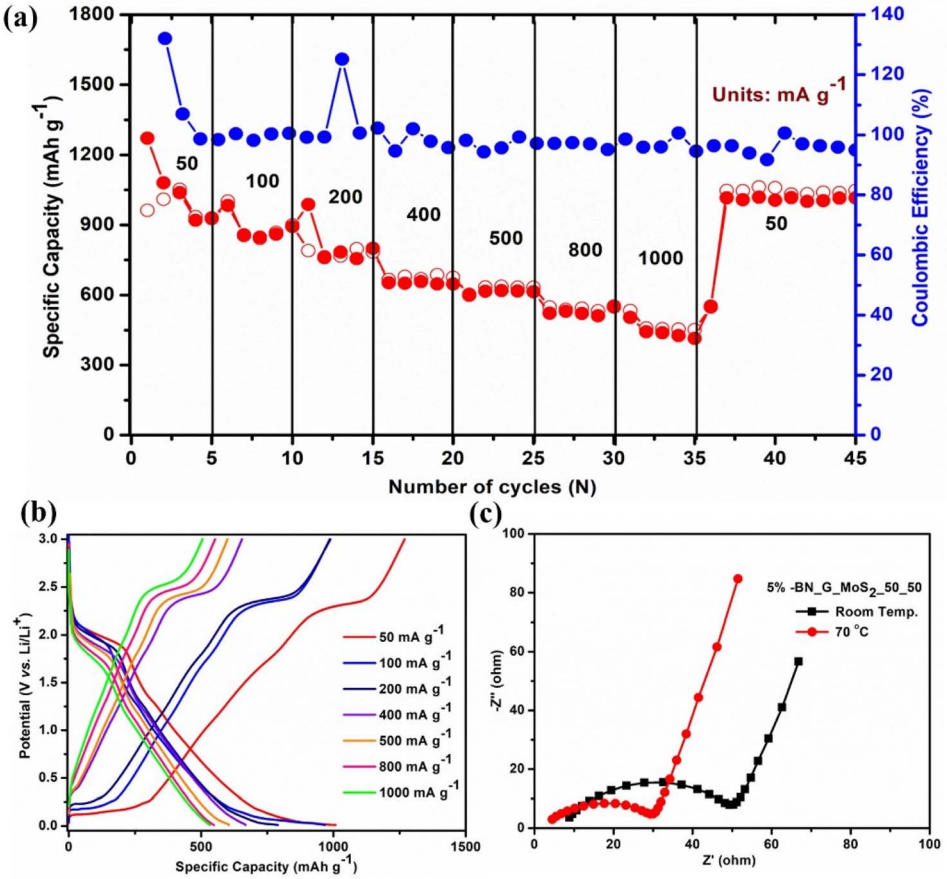

Fig. 8 (a) Rate performance, (b) galvanostatic discharge–charge curves at high temperature and (c) Nyquist plot at room temperature and high temperature of the 5% BN-G@MoS_2-50@50 composite electrode.

Table 2 R_s and R_{ct} values of 5% BN-G@MoS_2-10@90, 5% BN-G@MoS_2-50@50 and 5% BN-G@MoS_2-90@10 anodes before and after cycling

	Cycling			
	Before (Ω)		After (Ω)	
Name of the anodes	R_s	R_{ct}	R_s	R_{ct}
5% BN-G@MoS_2-10@90	20.8	72.1	28.1	63.8
5% BN-G@MoS_2-50@50	9.2	47.4	10.1	38.0
5% BN-G@MoS_2-90@10	7.9	38.3	17.1	87.3

Table 3 R_s and R_{ct} values of the 5% BN-G@MoS_2-50@50 anode at room temperature and high temperature

	Room temp. (Ω)		High temp. (Ω)	
Name of the anode	R_s	R_{ct}	R_s	R_{ct}
5% BN-G@MoS_2-50@50	8.5	50.3	4.2	29.1

after cycling the R_s and R_{ct} values were increased very little indicating the stability of the composite electrode. Consequently, we can draw the following conclusions about the stable capacity and rate performance at high temperatures: an enhanced h-BN thermal conductivity that results in a high Li^+ diffusion coefficient throughout the discharge process even at high temperatures, and a minor increase in electrode polarization because of the enhanced conductivity brought about by the addition of carbon.

5. Conclusion

This article describes the design and construction of 5% BN-graphene@MoS_2 composite electrodes, which were used as anode electrodes for lithium-ion batteries. The crystal structure and shape of these materials were validated by XRD and TEM. Additionally, the three composite electrodes 5% BN-G@MoS_2-10@90, 5% BN-G@MoS_2-50@50, and 5% BN-G@MoS_2-90@10 were subjected to an electrochemical investigation. Concerning reversible specific capacities, outstanding rate capability, and long-term (200 cycles) performance (765 mA h g^{-1} with a current density of 100 mA g^{-1}), 5% BN-G@MoS_2-50@50 exhibits the most promise of all the three anodes. More importantly, the 5% BN-G@MoS_2-50@50 composite electrode was studied at high rates at a high temperature (70 °C). Consequently, the best results for LIB anodes were obtained when operating at high temperatures, reaching a high capacity of 893.7 mA h g^{-1} at 100 mA g^{-1}. Even at a high current density of 1000 mA g^{-1}, a high capacity of 453 mA h g^{-1} was maintained. The enhanced electrochemical performance can be attributed to the combined actions of h-BN, MoS_2, and graphene sheets working in concert. Their better electrochemical performances point to the huge potential of the 5% BN-G@MoS_2-50@50 composite electrode in energy storage applications. Its widespread application in electrochemical energy storage devices guarantees its relevance in materials research for some time to come.

Data availability

The data that support the findings of this study are available from the corresponding author upon reasonable request.

Author contributions

All the authors have equal contribution.

Conflicts of interest

The authors declare that they have no conflict of interest.

Acknowledgements

The authors acknowledge the financial support for this work, which is part of the research project PIF 726175. The authors gratefully acknowledge Alfaisal University and its Office of Research & innovation for their continuous support throughout this study.

References

1 F. Qureshi, M. Yusuf, M. Tahir, M. Haq, M. M. I. Mohamed, H. Kamyab, H.-H. T. Nguyen, D.-V. N. Vo and H. Ibrahim, Renewable hydrogen production via biological and thermochemical routes: nanomaterials, economic analysis and challenges, *Process Saf. Environ. Prot.*, 2023, **179**, 68–88.
2 M. A. Hanif, F. Nadeem, R. Tariq and U. Rashid, *Renewable and Alternative Energy Resources*, Academic Press, 2021.
3 M. Tawalbeh, A. Farooq, R. Martis and A. Al-Othman, Optimization techniques for electrochemical devices for hydrogen production and energy storage applications, *Int. J. Hydrogen Energy*, 2024, **52**, 1058–1092.
4 Y. Wu, Q. Zhu and B. Zhu, Decoupling analysis of world economic growth and CO2 emissions: A study comparing developed and developing countries, *J. Cleaner Prod.*, 2018, **190**, 94–103.
5 R. M. Elavarasan, S. Afridhis, R. R. Vijayaraghavan, U. Subramaniam and M. Nurunnabi, SWOT analysis: A framework for comprehensive evaluation of drivers and barriers for renewable energy development in significant countries, *Energy Rep.*, 2020, **6**, 1838–1864.
6 M. Mitra, N. R. Singha and P. K. Chattopadhyay, Review on renewable energy potential and capacities of South Asian countries influencing sustainable environment: A comparative assessment, *Sustain. Energy Technol. Assessments*, 2023, **57**, 103295.
7 S. Algarni, V. Tirth, T. Alqahtani, S. Alshehery and P. Kshirsagar, Contribution of renewable energy sources to the environmental impacts and economic benefits for sustainable development, *Sustain. Energy Technol. Assessments*, 2023, **56**, 103098.

8 M. Asif, Renewable Energy: Technologies, Applications and Trends, *Handbook of Energy and Environment in the 21st Century*, CRC Press, 2024, pp. 41–65.
9 J. Zheng, J. Du, B. Wang, J. J. Klemeš, Q. Liao and Y. Liang, A hybrid framework for forecasting power generation of multiple renewable energy sources, *Renewable Sustainable Energy Rev.*, 2023, **172**, 113046.
10 Y. Chen, Y. Kang, Y. Zhao, L. Wang, J. Liu, Y. Li, Z. Liang, X. He, X. Li, N. Tavajohi and B. Li, A review of lithium-ion battery safety concerns: The issues, strategies, and testing standards, *J. Energy Chem.*, 2021, **59**, 83–99, DOI: **10.1016/j.jechem.2020.10.017**.
11 W. Liu, T. Placke and K. T. Chau, Overview of batteries and battery management for electric vehicles, *Energy Rep.*, 2022, **8**, 4058–4084, DOI: **10.1016/j.egyr.2022.03.016**.
12 P. Simon and Y. Gogotsi, Materials for electrochemical capacitors, *Nat. Mater.*, 2008, **7**, 845–854.
13 K. T. Nam, D.-W. Kim, P. J. Yoo, C.-Y. Chiang, N. Meethong, P. T. Hammond, Y.-M. Chiang and A. M. Belcher, Virus-enabled synthesis and assembly of nanowires for lithium ion battery electrodes, *Science*, 2006, **312**, 885–888.
14 A. Magasinski, P. Dixon, B. Hertzberg, A. Kvit, J. Ayala and G. Yushin, High-performance lithium-ion anodes using a hierarchical bottom-up approach, *Nat. Mater.*, 2010, **9**, 353–358.
15 Z.-Y. Gu, J.-M. Cao, K. Li, J.-Z. Guo, X.-T. Wang, S.-H. Zheng, X.-X. Zhao, B. Li, S.-Y. Li, W.-L. Li and X.-L. Wu, 2D Exfoliation Chemistry Towards Covalent Pseudo-Layered Phosphate Framework Derived by Radical/Strain-Synergistical Process, *Angew. Chem., Int. Ed.*, 2024, **63**, e202402371.
16 X.-T. Zhao, J.-Z. Guo, W.-L. Li, J.-P. Zhang and X.-L. Wu, Two-dimensional conjugated coordination polymer monolayer as anode material for lithium-ion batteries: A DFT study, *Chin. Chem. Lett.*, 2024, **35**, 108715, DOI: **10.1016/j.cclet.2023.108715**.
17 J.-M. Cao, I. V. Zatovsky, Z.-Y. Gu, J.-L. Yang, X.-X. Zhao, J.-Z. Guo, H. Xu and X.-L. Wu, Two-dimensional MXene with multidimensional carbonaceous matrix: A platform for general-purpose functional materials, *Prog. Mater. Sci.*, 2023, **135**, 101105, DOI: **10.1016/j.pmatsci.2023.101105**.
18 J. Mei, G. A. Ayoko, C. Hu, J. M. Bell and Z. Sun, Two-dimensional fluorine-free mesoporous Mo2C MXene via UV-induced selective etching of Mo2Ga2C for energy storage, *Sustainable Mater. Technol.*, 2020, **25**, e00156, DOI: **10.1016/j.susmat.2020.e00156**.
19 Z. Bao, C. Lu, X. Cao, P. Zhang, L. Yang, H. Zhang, D. Sha, W. He, W. Zhang, L. Pan and Z. Sun, Role of MXene surface terminations in electrochemical energy storage: A review, *Chin. Chem. Lett.*, 2021, **32**, 2648–2658, DOI: **10.1016/j.cclet.2021.02.012**.
20 S. Chen, J. Xu, M. Shi, Y. Yu, Q. Xu, X. Duan, Y. Gao and L. Lu, Polydopamine bridged MXene and NH2-MWCNTs nanohybrid for high-performance electrochemical sensing of Acetaminophen, *Appl. Surf. Sci.*, 2021, **570**, 151149, DOI: **10.1016/j.apsusc.2021.151149**.
21 H. Wang, S.-A. He, Z. Cui, C. Xu, J. Zhu, Q. Liu, G. He, W. Luo and R. Zou, Enhanced kinetics and efficient activation of sulfur by ultrathin MXene coating S-CNTs porous sphere for highly stable and fast charging lithium-sulfur batteries, *Chem. Eng. J.*, 2021, **420**, 129693, DOI: **10.1016/j.cej.2021.129693**.
22 Q. Su, J. Xie, J. Zhang, Y. Zhong, G. Du and B. Xu, In situ transmission electron microscopy observation of electrochemical behavior of CoS2 in lithium-ion battery, *ACS Appl. Mater. Interfaces*, 2014, **6**, 3016–3022.
23 Q. Wang, R. Zou, W. Xia, J. Ma, B. Qiu, A. Mahmood, R. Zhao, Y. Yang, D. Xia and Q. Xu, Facile Synthesis of Ultrasmall CoS2 Nanoparticles within Thin N-Doped Porous Carbon Shell for High Performance Lithium-Ion Batteries, *Small*, 2015, **11**, 2511–2517.
24 Q. Wang, L. Jiao, Y. Han, H. Du, W. Peng, Q. Huan, D. Song, Y. Si, Y. Wang and H. Yuan, CoS2 hollow spheres: fabrication and their application in lithium-ion batteries, *J. Phys. Chem. C*, 2011, **115**, 8300–8304.
25 B. Li, R. Wang, Z. Chen, D. Sun, F. Fang and R. Wu, Embedding heterostructured MnS/Co 1− x S nanoparticles in porous carbon/graphene for superior lithium storage, *J. Mater. Chem. A*, 2019, **7**, 1260–1266.
26 S. Gao, G. Chen, Y. Dall'Agnese, Y. Wei, Z. Gao and Y. Gao, Flexible MnS–Carbon Fiber Hybrids for Lithium-Ion and Sodium-Ion Energy Storage, *Chem. –A Euro. J.*, 2018, **24**, 13535–13539.
27 X. Cao, Y. Shi, W. Shi, X. Rui, Q. Yan, J. Kong and H. Zhang, Preparation of MoS2-coated three-dimensional graphene networks for high-performance anode material in lithium-ion batteries, *Small*, 2013, **9**, 3433–3438.
28 T. Wang, S. Chen, H. Pang, H. Xue and Y. Yu, MoS2-based nanocomposites for electrochemical energy storage, *Advanced Science*, 2017, **4**, 1600289.
29 W. Zhang, P. Zhang, Z. Su and G. Wei, Synthesis and sensor applications of MoS 2-based nanocomposites, *Nanoscale*, 2015, **7**, 18364–18378.
30 T. Stephenson, Z. Li, B. Olsen and D. Mitlin, Lithium ion battery applications of molybdenum disulfide (MoS 2) nanocomposites, *Energy Environ. Sci.*, 2014, **7**, 209–231.
31 X. Wei, C.-C. Lin, C. Wu, N. Qaiser, Y. Cai, A.-Y. Lu, K. Qi, J.-H. Fu, Y.-H. Chiang and Z. Yang, Three-dimensional hierarchically porous MoS2 foam as high-rate and stable lithium-ion battery anode, *Nat. Commun.*, 2022, **13**, 6006.
32 Y. Teng, H. Zhao, Z. Zhang, Z. Li, Q. Xia, Y. Zhang, L. Zhao, X. Du, Z. Du and P. Lv, MoS2 nanosheets vertically grown on graphene sheets for lithium-ion battery anodes, *ACS Nano*, 2016, **10**, 8526–8535.
33 B. G. Sook, N. K. Woo, K. J. Yun, S. Jongwoo, C. J. Wook and C. Sung-Yool, Effective Liquid-Phase Exfoliation and Sodium Ion Battery Application of MoS2 Nanosheets, *ACS Appl. Mater. Interfaces*, 2014, **6**, 7084–7089.
34 K. Chang and W. Chen, In situ synthesis of MoS 2/graphene nanosheet composites with extraordinarily high electrochemical performance for lithium ion batteries, *Chem. Commun.*, 2011, **47**, 4252–4254.

35 D. Xie, D. Wang, W. Tang, X. Xia, Y. Zhang, X. Wang, C. Gu and J. Tu, Binder-free network-enabled MoS2-PPY-rGO ternary electrode for high capacity and excellent stability of lithium storage, *J. Power Sources*, 2016, **307**, 510–518.

36 J. Wang, J. Liu, D. Chao, J. Yan, J. Lin and Z. X. Shen, Self-assembly of honeycomb-like MoS2 nanoarchitectures anchored into graphene foam for enhanced lithium-ion storage, *Adv. Mater.*, 2014, **26**, 7162–7169.

37 K. Chang and W. Chen, L-cysteine-assisted synthesis of layered MoS2/graphene composites with excellent electrochemical performances for lithium ion batteries, *ACS Nano*, 2011, **5**, 4720–4728.

38 Y. Liu, Y. Zhao, L. Jiao and J. Chen, A graphene-like MoS 2/graphene nanocomposite as a highperformance anode for lithium ion batteries, *J. Mater. Chem. A*, 2014, **2**, 13109–13115.

39 C. Wang, W. Wan, Y. Huang, J. Chen, H. H. Zhou and X. X. Zhang, Hierarchical MoS 2 nanosheet/active carbon fiber cloth as a binder-free and free-standing anode for lithium-ion batteries, *Nanoscale*, 2014, **6**, 5351–5358.

40 K. Chang, W. Chen, L. Ma, H. Li, H. Li, F. Huang, Z. Xu, Q. Zhang and J.-Y. Lee, Graphene-like MoS 2/amorphous carbon composites with high capacity and excellent stability as anode materials for lithium ion batteries, *J. Mater. Chem.*, 2011, **21**, 6251–6257.

41 Z. Wan, J. Shao, J. Yun, H. Zheng, T. Gao, M. Shen, Q. Qu and H. Zheng, Core–shell structure of hierarchical quasi-hollow MoS2 microspheres encapsulated porous carbon as stable anode for Li-ion batteries, *Small*, 2014, **10**, 4975–4981.

42 L. Zhang and X. W. Lou, Hierarchical MoS2 shells supported on carbon spheres for highly reversible lithium storage, *Chem. –A Euro. J.*, 2014, **20**, 5219–5223.

43 Y. Shi, Y. Wang, J. I. Wong, A. Y. S. Tan, C.-L. Hsu, L.-J. Li, Y.-C. Lu and H. Y. Yang, Self-assembly of hierarchical MoSx/CNT nanocomposites (2< x< 3): towards high performance anode materials for lithium ion batteries, *Sci. Rep.*, 2013, **3**, 2169.

44 S. Wu, R. Xu, M. Lu, R. Ge, J. Iocozzia, C. Han, B. Jiang and Z. Lin, Graphene-containing nanomaterials for lithium-ion batteries, *Adv. Energy Mater.*, 2015, **5**, 1500400.

45 L. Ma, J. Ye, W. Chen, D. Chen and J. Y. Lee, Gemini surfactant assisted hydrothermal synthesis of nanotile-like MoS2/graphene hybrid with enhanced lithium storage performance, *Nano Energy*, 2014, **10**, 144–152.

46 L. Ma, X. Zhou, L. Xu, X. Xu, L. Zhang and W. Chen, Chitosan-assisted fabrication of ultrathin MoS2/graphene heterostructures for Li-ion battery with excellent electrochemical performance, *Electrochim. Acta*, 2015, **167**, 39–47.

47 Z. Wang, T. Chen, W. Chen, K. Chang, L. Ma, G. Huang, D. Chen and J. Y. Lee, CTAB-assisted synthesis of single-layer MoS 2–graphene composites as anode materials of Li-ion batteries, *J. Mater. Chem. A*, 2013, **1**, 2202–2210.

48 J. Guo, X. Chen, S. Jin, M. Zhang and C. Liang, Synthesis of graphene-like MoS2 nanowall/graphene nanosheet hybrid materials with high lithium storage performance, *Catal. Today*, 2015, **246**, 165–171.

49 M. Örnek, C. Hwang, S. Xiang, K. Y. Xie, A. Etzold, B. Yang and R. A. Haber, Effect of synthesis conditions of BCNO on the formation and structural ordering of boron nitride at high temperatures, *J. Solid State Chem.*, 2019, **269**, 212–219.

50 B. Karupppaiah, A. Jeyaraman, S.-M. Chen and Y.-C. Huang, Development of highly sensitive electrochemical sensor for antibiotic drug ronidazole based on spinel cobalt oxide nanorods embedded with hexagonal boron nitride, *Electrochim. Acta*, 2023, **446**, 142008.

51 W. Luo, L. Zhou, K. Fu, Z. Yang, J. Wan, M. Manno, Y. Yao, H. Zhu, B. Yang and L. Hu, A thermally conductive separator for stable Li metal anodes, *Nano Lett.*, 2015, **15**, 6149–6154.

52 S. Angizi, S. A. A. Alem and A. Pakdel, Towards integration of two-dimensional hexagonal boron nitride (2D h-BN) in energy conversion and storage devices, *Energies*, 2022, **15**, 1162.

53 K. Zhang, Y. Feng, F. Wang, Z. Yang and J. Wang, Two dimensional hexagonal boron nitride (2D-hBN): synthesis, properties and applications, *J. Mater. Chem. C*, 2017, **5**, 11992–12022.

54 M. F. Rodrigues, K. Kalaga, H. Gullapalli, G. Babu, A. L. M. Reddy and P. M. Ajayan, Hexagonal boron nitride-based electrolyte composite for Li-ion battery operation from room temperature to 150 C, *Adv. Energy Mater.*, 2016, **6**, 1600218.

55 P. Arora and Z. Zhang, Battery separators, *Chem. Rev.*, 2004, **104**, 4419–4462.

56 X. Zhang, L. Ji, O. Toprakci, Y. Liang and M. Alcoutlabi, Electrospun nanofiber-based anodes, cathodes, and separators for advanced lithium-ion batteries, *Polym. Rev.*, 2011, **51**, 239–264.

57 H. Wu, D. Zhuo, D. Kong and Y. Cui, Improving battery safety by early detection of internal shorting with a bifunctional separator, *Nat. Commun.*, 2014, **5**, 5193.

58 Y. Feng, G. Han, B. Wang, X. Zhou, J. Ma, Y. Ye, C. Liu and X. Xie, Multiple synergistic effects of graphene-based hybrid and hexagonal born nitride in enhancing thermal conductivity and flame retardancy of epoxy, *Chem. Eng. J.*, 2020, **379**, 122402.

59 S. T. Gunday, E. Cevik, A. Yusuf and A. Bozkurt, Nanocomposites composed of sulfonated polysulfone/hexagonal boron nitride/ionic liquid for supercapacitor applications, *J. Energy Storage*, 2019, **21**, 672–679.

60 L. Yu, P. L. Yap, A. Santos, D. Tran, K. Hassan, J. Ma and D. Losic, Graphene and Hexagonal Boron Nitride in Molybdenum Disulfide/Epoxy Composites for Significant X-ray Shielding Enhancement, *ACS Appl. Nano Mater.*, 2022, **5**, 12196–12208.

61 C. S. Bongu, M. Arsalan and E. H. Alsharaeh, 2D Hybrid Nanocomposite Materials (h-BN/G/MoS2) as a High-Performance Supercapacitor Electrode, *ACS Omega*, 2024, **9**, 15294–15303.

62 C. S. Bongu, Y. Mussa, S. Aleid, M. Arsalan and E. H. Alsharaeh, SnO2/h-BN Nanocomposite Modified Separator as High-Efficiency Polysulfide Trap in Lithium-Sulfur Battery, *Energy Adv.*, 2023, **2**, 1926–1934.

63 N. Althubaiti, Y. Mussa, C. S. Bongu, Z. Bayhan, M. Arsalan, A. Soliman and E. Alsharaeh, Reduced graphene oxide/hexagonal boron nitride-based composite as a positive electrode in asymmetric supercapacitors, *J. Mater. Sci.*, 2022, **57**, 14371–14385.

64 Y. Tang, D. Wu, Y. Mai, H. Pan, J. Cao, C. Yang, F. Zhang and X. Feng, A two-dimensional hybrid with molybdenum disulfide nanocrystals strongly coupled on nitrogen-enriched graphene via mild temperature pyrolysis for high performance lithium storage, *Nanoscale*, 2014, **6**, 14679–14685.

65 R. Zhou, J.-G. Wang, H. Liu, H. Liu, D. Jin, X. Liu, C. Shen, K. Xie and B. Wei, Coaxial MoS2@ carbon hybrid fibers: A low-cost anode material for high-performance Li-ion batteries, *Materials*, 2017, **10**, 174.

66 F. Zhou, S. Xin, H. Liang, L. Song and S. Yu, Carbon nanofibers decorated with molybdenum disulfide nanosheets: synergistic lithium storage and enhanced electrochemical performance, *Angew. Chem., Int. Ed.*, 2014, **53**, 11552–11556.

67 U. K. Sen and S. Mitra, High-Rate and High-Energy-Density Lithium-Ion Battery Anode Containing 2D MoS2 Nanowall and Cellulose Binder, *ACS Appl. Mater. Interfaces*, 2013, **5**, 1240–1247, DOI: **10.1021/am3022015**.

68 C. Chen, X. Xie, B. Anasori, A. Sarycheva, T. Makaryan, M. Zhao, P. Urbankowski, L. Miao, J. Jiang and Y. Gogotsi, MoS2-on-MXene Heterostructures as Highly Reversible Anode Materials for Lithium-Ion Batteries, *Angew. Chem., Int. Ed.*, 2018, **57**, 1846–1850, DOI: **10.1002/anie.201710616**.

69 Y. Liu, D. Tang, H. Zhong, Q. Zhang, J. Yang and L. Zhang, A novel MoS2/C nanocomposite as an anode material for lithium-ion batteries, *J. Alloys Compd.*, 2017, **729**, 583–589, DOI: **10.1016/j.jallcom.2017.09.201**.

70 B. Chen, E. Liu, T. Cao, F. He, C. Shi, C. He, L. Ma, Q. Li, J. Li and N. Zhao, Controllable graphene incorporation and defect engineering in MoS2-TiO2 based composites: Towards high-performance lithium-ion batteries anode materials, *Nano Energy*, 2017, **33**, 247–256, DOI: **10.1016/j.nanoen.2017.01.034**.

71 C. Zhao, J. Kong, X. Yao, X. Tang, Y. Dong, S. L. Phua and X. Lu, Thin MoS2 Nanoflakes Encapsulated in Carbon Nanofibers as High-Performance Anodes for Lithium-Ion Batteries, *ACS Appl. Mater. Interfaces*, 2014, **6**, 6392–6398, DOI: **10.1021/am4058088**.

72 B. Liu, F. Li, H. Li, S. Zhang, J. Liu, X. He, Z. Sun, Z. Yu, Y. Zhang, X. Huang, F. Guo, G. Wang and X. Jia, Monodisperse MoS2/Graphite Composite Anode Materials for Advanced Lithium Ion Batteries, *Molecules*, 2023, **28**, 2775.

73 M. Faizan, S. Hussain, M. Islam, J.-Y. Kim, D. Han, J.-H. Bae, D. Vikraman, B. Ali, S. Abbas, H.-S. Kim, A. N. Singh, J. Jung and K.-W. Nam, MoO3@MoS2 Core-Shell Structured Hybrid Anode Materials for Lithium-Ion Batteries, *Nanomaterials*, 2022, **12**, 2008.

74 M. Faizan, S. Hussain, D. Vikraman, B. Ali, H.-S. Kim, J. Jung and K.-W. Nam, MoS2@Mo2C hybrid nanostructures formation as an efficient anode material for lithium-ion batteries, *J. Mater. Res. Technol.*, 2021, **14**, 2382–2393, DOI: **10.1016/j.jmrt.2021.07.127**.

75 C. Zhao, J. Fu, A. Shen, L. Zhang, S. Kong, Y. Feng, W. Gong, K. Tian and Q. Li, Interfacial coupling of MoS2/MoO3 hierarchical heterostructures as superior anodes for high-performance lithium-ion battery, *J. Energy Storage*, 2023, **72**, 108595, DOI: **10.1016/j.est.2023.108595**.

76 F. Zhang, K. Németh, J. Bareño, F. Dogan, I. D. Bloom and L. L. Shaw, Experimental and theoretical investigations of functionalized boron nitride as electrode materials for Li-ion batteries, *RSC Adv.*, 2016, **6**, 27901–27914, DOI: **10.1039/C6RA03141B**.

77 L. Ji, Z. Lin, M. Alcoutlabi and X. Zhang, Recent developments in nanostructured anode materials for rechargeable lithium-ion batteries, *Energy Environ. Sci.*, 2011, **4**, 2682–2699.

78 C. Li, Z. Li, Q. Li, Z. Zhang, S. Dong and L. Yin, MOFs derived hierarchically porous TiO2 as effective chemical and physical immobilizer for sulfur species as cathodes for high-performance lithium-sulfur batteries, *Electrochim. Acta*, 2016, **215**, 689–698.

79 J. Jang, Y. Kim, O. B. Chae, T. Yoon, S. Kim, H. Kim, H. Park, J. H. Ryu and S. M. Oh, A First-Cycle Coulombic Efficiency Higher than 100% Observed for a Li2MO3 (M= Mo or Ru) Electrode, *Angew. Chem., Int. Ed.*, 2014, **53**, 10654–10657.

80 P. Periasamy, T. Krishnakumar, V. Devarajan, M. Sandhiya, M. Sathish and M. Chavali, Investigation of electrochemical supercapacitor performance of WO3-CdS nanocomposites in 1 M H2SO4 electrolyte prepared by microwave-assisted method, *Mater. Lett.*, 2020, **274**, 127998.

81 K. Dhamodharan and A. K. Singh, Coupled interaction of exfoliated hexagonal boron nitride nanosheets decorated with MoS2 nanoflowers to enrich electrochemical activities for hybrid supercapacitor applications, *J. Alloys Compd.*, 2024, 174732.

82 M.-T. F. Rodrigues, K. Kalaga, H. Gullapalli, G. Babu, A. L. M. Reddy and P. M. Ajayan, Hexagonal Boron Nitride-Based Electrolyte Composite for Li-Ion Battery Operation from Room Temperature to 150 °C, *Adv. Energy Mater.*, 2016, **6**, 1600218, DOI: **10.1002/aenm.201600218**.